Cancer Research

Tipifarnib Inhibits HRAS-Driven Dedifferentiated Thyroid Cancers

Brian R. Untch[1,2], Vanessa Dos Anjos[1], Maria E.R. Garcia-Rendueles[1], Jeffrey A. Knauf[1], Gnana P. Krishnamoorthy[1], Mahesh Saqcena[1], Umeshkumar K. Bhanot[3], Nicholas D. Socci[4], Alan L. Ho[5,6], Ronald Ghossein[7], and James A. Fagin[1,5,6]

Abstract

Of the three RAS oncoproteins, only HRAS is delocalized and inactivated by farnesyltransferase inhibitors (FTI), an approach yet to be exploited clinically. In this study, we treat mice bearing Hras-driven poorly differentiated and anaplastic thyroid cancers (*Tpo-Cre/Hras*^{G12V}*/p53*$^{flox/flox}$) with the FTI tipifarnib. Treatment caused sustained tumor regression and increased survival; however, early and late resistance was observed. Adaptive reactivation of RAS–MAPK signaling was abrogated *in vitro* by selective RTK (i.e., EGFR, FGFR) inhibitors, but responses were ineffective *in vivo*, whereas combination of tipifarnib with the MEK inhibitor AZD6244 improved outcomes. A subset of tumor-bearing mice treated with tipifarnib developed acquired resistance. Whole-exome sequencing of resistant tumors identified a *Nf1* nonsense mutation and an activating mutation in *Gnas* at high allelic frequency, supporting the on-target effects of the drug. Cell lines modified with these genetic lesions recapitulated tipifarnib resistance *in vivo*. This study demonstrates the feasibility of targeting Ras membrane association in cancers *in vivo* and predicts combination therapies that confer additional benefit.

Significance: Tipifarnib effectively inhibits oncogenic HRAS-driven tumorigenesis and abrogating adaptive signaling improves responses. NF1 and GNAS mutations drive acquired resistance to Hras inhibition, supporting the on-target effects of the drug. *Cancer Res; 78(16); 4642–57.* ©*2018 AACR.*

Introduction

Development of compounds that inhibit oncogenic RAS remains a major unfulfilled challenge. As opposed to activating kinase mutations, which enable small-molecule targeting of their enzymatic activity, RAS mutants lose GTPase function, resulting in reduced GTP hydrolysis and activation of downstream signaling. Pharmacologic targeting of GDP/GTP exchange and inhibition of Ras–effector interactions have not proven so far to be effective strategies (1). Recently, a series of KRAS-G12C–specific inhibitors that bind covalently to the mutant cysteine residue have shown promise and are in preclinical development (2).

Although oncogenic *HRAS* mutations are comparatively less frequent than those of *K* and *NRAS*, they are significantly represented in follicular thyroid cell–derived and in medullary thyroid carcinomas, as well as in head and neck and bladder cancers (3–8). HRAS is the only RAS oncoprotein that can be pharmacologically inhibited through membrane delocalization by farnesyltransferase inhibitors (FTI). This is because upon farnesyltransferase inhibition, N- and K-, but not HRAS, are geranyl-geranylated, and hence remain membrane anchored and functional (9). Accordingly, FTIs are preferentially active against *HRAS* as compared with *NRAS*- or *KRAS*-mutant cancer cell lines (9–11). FTIs were originally developed to target RAS but were ineffective in clinical trials (12, 13). However, these studies did not attempt to enroll patients with *HRAS*-driven cancers, and hence the efficacy of targeting the association of RAS with membranes has not been formally tested in patients, or in genetically accurate mouse models of Hras-driven cancer.

The FTI lonafarnib has been previously shown to preferentially inhibit growth of *HRAS*-mutant cancer cell lines, and to essentially eliminate *Hras*^{G12V}-driven papillomas in mice (10). We developed a mouse model of *Hras*^{G12V}-driven cancer that phenocopies poorly differentiated or anaplastic thyroid cancers, and used this to test the efficacy, adaptive and acquired responses to the FTI tipifarnib. The drug evoked strong antitumor responses, but both early and delayed resistance ensued. Adaptive resistance to tipifarnib was associated with upstream activation of receptor tyrosine kinases (RTK), primarily EGFR and FGFR1. Combination with a MEK inhibitor, but not with the RTK inhibitors erlotinib or ponatinib, markedly improved

[1]Human Oncology and Pathogenesis Program, Memorial Sloan Kettering Cancer Center, New York, New York. [2]Department of Surgery, Memorial Sloan Kettering Cancer Center, New York, New York. [3]Pathology Core Facility, Memorial Sloan Kettering Cancer Center, New York, New York. [4]Marie-Josée & Henry R. Kravis Center for Molecular Oncology and Bioinformatics Core, Memorial Sloan Kettering Cancer Center, New York, New York. [5]Department of Medicine, Memorial Sloan Kettering Cancer Center, New York, New York. [6]Department of Medicine, Weill Cornell Medical College, New York, New York. [7]Department of Pathology, Memorial Sloan Kettering Cancer Center, New York, New York.

Note: Supplementary data for this article are available at Cancer Research Online (http://cancerres.aacrjournals.org/).

Corresponding Author: James A. Fagin, Department of Medicine and Human Oncology and Pathogenesis Program, Memorial Sloan-Kettering Cancer Center, 1275 York Avenue, New York, NY 10065. Phone: 646-888-2164; Fax: 646-422-0675; E-mail: faginj@mskcc.org

doi: 10.1158/0008-5472.CAN-17-1925

in vivo responses to tipifarnib, consistent with heterogeneity of the adaptive inputs upstream of Ras. Individual cases of acquired resistance to tipifarnib were driven by *Nf1* loss, resulting in reactivation of Ras signaling, and by activating *Gnas* mutations, which induced a transcriptional program of redifferentiation.

Materials and Methods

Genetically engineered mice and mouse tumor cell lines

All animal protocols were approved by the MSKCC Institutional Animal Care and Use Committee. To generate triple transgenic (*Hras;p53*) mice we crossed animals harboring *Tpo-Cre* (14), *Trp53*^{flox} (15), and *FR-Hras*^{G12V} (16) alleles (mixed background containing 129, Swiss black, FVB/n and C57bl6). Thyroid ultrasound (VisualSonics Vevo 770 In Vivo High-Resolution Micro-Imagin System, VisualSonics Inc.) was performed after isoflurane anesthesia and hair removal. The neck was imaged from above the larynx through the thoracic inlet with image capture every 250 μm and subsequent volume determination. Tumor-bearing animals were defined as having an identifiable tumor extending outside the normal thyroid bed. Total thyroid volume was used to assess the thyroid as the boundaries of the tumors were often difficult to clearly delineate by ultrasound and as they could also involve both thyroid lobes.

Cell culture and reagents

To generate mouse tumor cell lines, tumors were dissected, minced in PBS, and resuspended in 10 mL of digestion minimum essential media (MEM) containing collagenase type I (112 U/mL; Worthington; #CLS-1), dispase (1.2 U/mL; Gibco; #17105-041), penicillin (50 U/mL), and streptomycin (50 μg/mL). Cells were incubated at 37°C for 60 minutes with vigorous shaking and then passed through a 10-mL pipette followed by an additional 60 minutes of shaking. Cells were spun down and resuspended in Coon F12 with penicillin/streptomycin/L-glutamine (P/S/G; Gemini; #400-110) and 0.5% bovine brain extract for two weeks and then switched to Coon F12 with P/S/G in 5% FBS. Lines were passaged at least five times prior to use in experiments.

Hth83 and C643 human cancer cell lines were obtained from Nils-Erik Heldin, Uppsala University Hospital (Uppsala, Sweden). Prior to experiments, they were authenticated using short tandem repeat and SNP array analysis and tested negative for *Mycoplasma*. They were grown in RPMI1640 supplemented with 10% FBS and P/S/G. HEK293FT and Platinum-E (PlatE) cell lines were grown in DMEM-HG and DMEM, respectively, and all cells were incubated at 37°C in a 5% CO_2 incubator.

All drugs used *in vivo* were administered by gavage. Tipifarnib (Kura Oncology) and erlotinib (Selleckchem) were dissolved in 20% 2-hydroxypropyl-β-cyclodextrin (CTD, Inc), which also served as vehicle. AZD6244 (AstraZeneca) was dissolved in 0.5% methycellulose and 0.1% Tween80. Ponatinib (AK Scientific, Inc.) was dissolved in 25 mmol/L citric acid buffer. All tumors were collected 2 hours after last dose of drug. Tumor-bearing mice were identified by ultrasound, then stratified by sex and tumor size/thyroid volume and then randomized to treatment groups.

Histology, IHC, and immunofluorescence

After CO_2 anesthesia, thyroid tumors were dissected from surrounding tissues and placed in 4% paraformaldehyde (PFA) for 24 hours at 4°C. The specimens were washed twice with PBS and placed into 70% ethanol. Paraffin embedding, sectioning, deparaffinization, and staining were carried out by the MSKCC Molecular Cytology Core. Sections were immunostained with Iba-1 (Wako; 019-1974, 0.5 μg/mL), pERK (Cell Signaling Technology, #4370; 1.0 μg/mL), Ki67 (Abcam; Ab16667, 2.5 μg/mL), pAKT473 (Cell Signaling Technology #4060; 1.0 μg/mL). Quantitation of IHC was performed using color threshold analysis. Slides were scanned with Pannoramic Flash 250 (3DHistech) and regions of interest manually drawn using Pannoramic Viewer and exported as tiled tiff images. The images were analyzed using FIJI/ImageJ. A color deconvolution algorithm was used to separate 3,3′-diaminobenzidine (DAB) and hematoxylin signals. A set threshold value was used to segment positive DAB signal as well as tissue area. Percent of DAB signal over tissue area for each image was measured.

Immunofluorescence staining was performed using a Discovery XT processor (Ventana Medical Systems). Tumors were processed as above. Fixation of cell lines was performed on chamber slides exposed to 4% PFA for 30 minutes and washed with PBS. Slides were incubated first with anti-vimentin (Progen; # GP53; 0.1 μg/mL) for 5 hours, followed by 60-minute incubation with biotinylated goat anti-guinea pig IgG (Vector Laboratories; # BA-7000; 1:200). The detection was performed with Streptavidin-HRP D (DABMap kit, Ventana Medical Systems), followed by incubation with Tyramide Alexa Fluor 488 (Invitrogen; # T20922) prepared according to manufacturer's instruction with predetermined dilutions. Slides were then incubated with anti-E-cadherin (Cell Signaling Technology; #3195, 2.5 μg/mL) using the same protocol as vimentin except for an alternative secondary antibody (biotinylated goat anti-rabbit, Vector Laboratories; # PK6101, 1:200 dilution). After staining, slides were counterstained with 4′,6-diamidino-2-phenylindole (DAPI; Sigma Aldrich; # D9542; 5 μg/mL) for 10 minutes and mounted in Mowiol reagent.

Human tumor and cell line expression arrays

Thyroid cancer cell lines underwent RNA extraction and gene expression was measured with Affymetrix U133 2.0 arrays. We also mined publicly available human expression array data with the same platform from normal thyroid and thyroid tumors (GSE76039; ref. 17). Genotyping for mutant *RAS* or *BRAF* status was performed by targeted exome sequencing as described previously (17). Expression array data was normalized in Partek genomic Suite 6.6. The data was sorted for expression of RTKs (18) and RTK ligands.

Ligands and proliferation assays

For proliferation assays, 3×10^4 cells were seeded in 6-well plates. The day after plating (day 0), drugs/ligands were added. Media/drugs/ligands were replaced on day 3, and cells harvested on day 6 by trypsinization and counted with a Vi-Cell series Cell Viability Analyzer (Beckman Coulter). Ligand concentrations are listed in Supplementary Table S1.

Immunoblots and RAS-GTP assays

Cells were rinsed with cold PBS and lysed in Mg^{2+} lysis buffer (containing 125 mmol/L HEPES, pH 7.5, 750 mmol/L NaCl, 5% Igepal CA-630, 50 mmol/L $MgCl_2$, 5 mmol/L EDTA, and 10% glycerol; Millipore #20-168) supplemented with protease

inhibitors (Complete Mini, Roche) and phosphatase inhibitors (phosphatase inhibitor cocktail set I and II, Sigma). Tumors were homogenized in 1× Lysis/Binding/Wash Buffer (containing 25 mmol/L Tris-HCl, 150 mmol/L NaCl, 1% NP-40, 5% Glycerol, and 5 mmol/L $MgCl_2$; Thermo Fisher Scientific #1862301) also supplemented with protease/phosphatase inhibitors. Lysates were briefly sonicated to disrupt the tissue before clearing by centrifugation. The protein concentrations of the lysates were measured using the BCA Kit (Thermo Fisher Scientific) on a microplate reader (SpectraMax M5). Western blots were performed as described previously (19). Membranes were incubated with secondary goat anti-rabbit horseradish peroxidase (HRP)-conjugated antibody (1:5,000 or 1:7,500; Santa Cruz Biotechnology; sc-2004) or goat anti-mouse HRP-conjugated antibody (1:5,000 or 1:10,000; Santa Cruz Biotechnology; sc-2031) for 1 hour at room temperature. Blots were developed by chemiluminescence in Amersham ECL Prime (GE Healthcare Biosciences) or SuperSignal West Pico (Thermo Fisher Scientific) or Immobilon HRP (Millipore) reagents as per manufacturer's instructions. RAS-GTP was measured using the Active Ras Pull-Down and Detection Kit from Thermo Fisher Scientific (#16117) according to the manufacturer's protocol, followed by immunoblotting to detect GTP-bound levels of total RAS or RAS isoforms.

RNA interference

For siRNA-mediated knockdown of KRAS and NRAS, cells were transfected with 50 nmol/L of either the targeting or control siRNA (Qiagen) using Lipofectamine RNAiMAX (Invitrogen; #13778-100), following the manufacturer's protocol (Supplementary Table S2). After transfection, cells were incubated with DMSO or tipifarnib for 72 hours.

Quantitative real-time PCR and expression arrays

Total mRNA was extracted from cells and snap-frozen thyroid tissue with PrepEase Kit (USB Corporation). The amount and purity of RNA were determined by spectrophotometry (NanoDrop 2000, Thermo Fisher Scientific). RNA expression from *Tpo-Cre*, *Tpo-Cre/Hras*^{G12V} and *Hras;p53* PDTC/ATC was measured on Affymetrix GeneChip Mouse Genome 430 2.0 arrays (deposited in the GEO repository: GSE112476. Data were analyzed using Partek Genomic Suites 6.6. First-strand cDNA was synthesized using Super Script III First Strand Kit (Invitrogen) according to the manufacturer's protocol. Real-Time PCR was performed by using Power SYBR Green PCR Master Mix (Applied Biosystems) using the primers listed in Supplementary Table S3. For the analysis of expression, we used the $\Delta\Delta C_t$ method, using β-actin as the housekeeping gene.

Vectors, mutagenesis, and cell transfection

Short hairpins for human EGFR and NF1 were cloned into pMSCV-miRE vector and pLKO vector (MSKCC RNAi Core Facility), respectively. The Gnas plasmids were purchased from GeneCopoeia (EX-Mm27105-Lv205 for mouse). GNAS^{201} refers to the canonical GNAS sequence, $G\alpha_{S2}$. Gnas mutants were generated on the $G\alpha_{S1}$ cDNA, since expression of this transcript was the highest among those expressed from the *Gnas* complex locus in our models (NM_001077510). The GNAS^{R201S} position in human and mouse $G\alpha_{S2}$ corresponds to the following substitutions: GNAS^{R187S} in $G\alpha_{S1}$ and GNAS^{R940S} in Xlas-1 in both species. GNAS^{R160C} in $G\alpha_{S2}$ corresponds to GNAS^{R146S} in $G\alpha_{S1}$. To be consistent with the reported annotation in the literature, we refer throughout the manuscript to Gnas^{R201S} and Gnas^{R160C} mutations. The mutant *Gnas* cDNAs (Gnas^{R201S} and Gnas^{R160C}) were generated by site-directed mutagenesis. We introduced substitutions at the 201 and 160 sites using 50 ng of plasmid, Acuprime PFX (Invitrogen; 12344-040), using a PCR protocol. Forward and reverse primers used to introduce the mutations are shown in Supplementary Table S4. All plasmids were sequenced to confirm that the desired mutations were introduced. For Gnas, transient transfection of HEK293FT cells was performed by using the Lenti-Pac HIV Expression Packaging Kit (Genecopoeia; HPK-LvTR-20), 24 hours after cells were seeded (5×10^5/dish) in 60-mm dishes. For EGFR and NF1 hairpins, transient transfection of PlatE cells was performed using Fugene 6 transfection reagent (Promega); 24 hours later cells were seeded (2×10^6/dish) in 60-mm dishes, according to the manufacturer's protocol. For infections, cells were incubated with infectious particles twice in the presence of 8 μg/mL of polybrene (Santa Cruz Biotechnology; sc-134220). The medium was replaced 24 hours after the second infection with fresh medium containing 1.5–2.5 μg/mL puromycin (Millipore; 540411). Efficiency of knockdown was verified by immunoblotting.

To generate a myristoylated HRAS, NIH3T3 cells were transduced with either HRAS^{G12V} (NM_005346.3; Genecopoeia; CS-B0109-Lv205-01) or myristoylated HRAS^{G12V} (MGQSLT or ATGGGTCAATCTCTTACA; Genecopoeia; CS-B0109-Lv205-02) in a pReceiver-Lv205 plasmid. HEK239FT cells were transfected with plasmid, using the Lenti-Pac HIV Expression Packaging Kit, 48 hours after cells were seeded (1.5×10^6/dish) in 100-mm dishes. Lentivirus were collected 48 hours posttransfection and NIH3T3 cells were transduced in the presence of polybrene. After 72 hours posttransduction, 1.5 μg/mL puromycin was added to the medium and selected cells were used in proliferation assays.

CRISPR/Cas9 *Nf1* gene editing and selection

Single-guide RNAs targeting the NF1 binding domain in exon 39 were designed using the CRISPR design software program (http://crispr.mit.edu/) and ligated into *BsmBI*-linearized LentiCRISPR plasmid (gift from Feng Zhang via Addgene; #49535; ref. 20). *Hras;p53* PDTC cells (5×10^5 cells per 60-mm dish) were plated overnight, and transfected with 1 μg of LentiCRISPR plasmid using FuGene 6, selected under 2.5 μg/mL of puromycin for 48 hours and plated in a 150-mm dish (500 cells). Single-cell colonies were expanded for DNA and protein extraction, and proliferation assays. PCR primers spanning potential target sites of deletion were designed (F 5′-AAAGAATCGACCGTGCTTTG-3′, R 5′-ACAGGGTACCACAGACAAAAA-3′). Mutations were confirmed by Sanger sequencing.

Mouse genomics

Fresh frozen mouse tumors were laser capture microdissected in the Pathology Core Lab, Precision Pathology and Biospecimen Center of MSKCC using Leica LMD6. Tissue sections of 8–10 μm were placed on PEN membrane slides (Applied Biosystems) and stained with hematoxylin and eosin. Multiple serial sections of tissue were used to maximize yields. Collected cells were pooled together for DNA extraction. Array CGH and whole-exome sequencing were performed with Agilent 415K Mouse CGH arrays and SureSelect All Exon capture kit, respectively. We developed a

novel approach to aCGH-specific normalization to deal with a specific feature of aCGH microarray data as these profiles are subject to artifacts related to genomic regional labeling efficiency. These artifacts may result from regional variation in DNA degradation, fragmentation, methylation, or other features affecting sample DNA differently than reference DNA. Because the artifacts are regionally distributed, they can appear as regional increases and decreases in probe $\log_2$ ratios, mimicking copy number aberrations (CNA). Circular binary segmentation and other approaches cannot distinguish such artifacts, and they are typically segmented as altered regions. We have incorporated genomic artifact models based on %GC over 50 Kb, 2 Kb and 200 bp windows for quantitation of artifact during quality assurance and for removal using Loess during normalization. Segmentation files were analyzed using IGV 2.3.82.

Samples were prepared for whole-exome sequencing according to the manufacturer instructions. PCR amplification of the libraries was carried out for 6 cycles in the precapture step and for 8 cycles postcapture. Samples were barcoded and run on a Hiseq 2500/4000 in a 100 bp/100 bp paired-end run, using the TruSeq SBS Kit v3 (Illumina). The average coverage was 300× for the tumor samples and 116× for the normal samples. The data processing pipeline for detecting variants in Illumina HiSeq data is as follows: first, the FASTQ files are processed to remove any adapter sequences at the end of the reads using cutadapt (v1.6). The files are then mapped using the BWA mapper (bwa mem v0.7.12). After mapping, the SAM files are sorted and read group tags are added using the PICARD tools. After sorting in coordinate order, the BAM's are processed with PICARD MarkDuplicates. The marked BAM files are then processed using the GATK toolkit (v 3.2) according to best practices for tumor-normal pairs. They are first realigned using the InDel realigner and then the base quality values are recalibrated with the BaseQRecalibrator. Somatic variants are then called in the processed BAMs using muTect (v1.1.7). A more complete description and a full listing of the code used in this pipeline are available at https://github.com/soccin/BIC-variants_pipeline.

Xenografts/allografts

Cells at 70% confluency were trypsinized, resuspended in medium, and injected into the right flank of nude mice (5×10^6 cells per mouse). Treatment by gavage (see above for drug regimens) commenced when xenografts/allografts reached measurable volumes (≈100–300 mm^3). Xenograft volume was measured with calipers 2–3 times per week for 3 weeks and tumors collected 2 hours after last dosing. Tumors were placed immediately in either liquid N_2 or 4% PFA. For RNA-sequencing (RNA-seq), RNA extraction of frozen tissue was performed by the MSKCC Integrative Genomics Operation. After ribogreen quantification and quality control of Agilent BioAnalyzer, 500 ng of total RNA underwent polyA selection and Truseq library preparation according to instruction provided by Illumina (TruSeq RNA Sample Prep Kit v2), with 6 cycles of PCR. Samples were barcoded and run on a Hiseq 2500 in a 50 bp/50 bp paired end run, using the TruSeq SBS Kit v3 (Illumina). An average of 58 million paired reads was generated per sample. At most the ribosomal reads represented 0.1% and the percent of mRNA bases was closed to 66% on average. RNA-seq data was analyzed using GSEA (broadinstitute.org/gsea).

Statistical analysis

Statistical analysis was performed with GraphPad Prism version 7.0a. Two-tailed *t* tests were used for data with an assumed Gaussian distribution, whereas Mann–Whitney tests were used as nonparametric tests. Kaplan–Meier survival curves were analyzed with a log-rank test. Statistical significance was defined as a $P < 0.05$. IC_{50} values and curves were generated using nonlinear regression.

Antibodies

The following antibodies were used for immunoblots at a dilution of 1:1,000, except where indicated. HRAS (sc-520), NRAS (sc-31; 1:500), KRAS (sc-30; 1:500), FRS2 (sc-8318), CREB (sc-58), and GFP (sc-9996) were from Santa Cruz Biotechnology; pMEK S217/221 (#9121), tMEK (#9122), pERK (#9101), tERK (#4695), FGFR1 (#9740), pFRS2 (#3864), pAKT (#9271), EGFR (#4267), pEGFR (#3777), and pCREB (#9198) were from Cell Signaling Technology; β-actin (A2228; 1:10,000) and Vinculin (V4139) were from Sigma; and NF1 (A300-140A-M) was from Bethyl Laboratories.

Results

Mice with thyroid-specific inactivation of *p53* and knock-in of $Hras^{G12V}$ develop aggressive thyroid cancers

Mutations of *TP53* are genomic hallmarks of advanced forms of thyroid cancer (17). To derive a dedifferentiated, Ras-driven thyroid cancer model, we developed mice harboring flox-and-replace $Hras^{G12V}$ and floxed *p53* alleles ($p53^{f}$), selectively disrupted in thyrocytes through a *Tpo-Cre* transgene (Fig. 1A). *Tpo-Cre*/$Hras^{G12V+/+}$, *Tpo-Cre*/$Hras^{G12V+/-}$, or *Tpo-Cre*/$p53^{f/f}$ mice failed to generate thyroid tumors, but when combined (*Hras;p53*) produced aggressive tumors that recapitulated the histologic characteristics of human poorly differentiated (PDTC) or anaplastic thyroid cancers (ATC). ATCs were characterized by spindle-shaped cells with loss of E-cadherin and increased vimentin expression, whereas PDTCs had focal necrosis and tightly packed groups of E-cadherin–positive cuboidal cells (Fig. 1B). We generated cell lines from these two distinct tumor types, and found that they consistently retained their original epithelial/mesenchymal characteristics *in vitro* (Fig. 1B).Tumor-bearing mice had a 50% mortality by approximately 40 weeks (Supplementary Fig. S1A). Doubling time for ATCs was consistently short (8.8 ± 0.97 days), whereas in PDTCs it was more variable (18.1 ± 4.8; Supplementary Fig. S1B). *Hras;p53* tumors had reduced or absent expression of the thyroid-specific genes *Nis, Tg, Tpo*, and *Tshr*. The thyroid lineage transcription factor *Pax8* was also partially suppressed, whereas *Nkx2.1* (*Ttf1*) was not affected (Supplementary Fig. S1C). The expression of the MAPK transcription output markers *Fosl1 and Hmga2* (21) tended to be higher in ATCs than PDTCs (Fig. 1C), consistent with findings from their human counterparts (17). Array comparative genomic hybridization (aCGH) of *Hras;p53* PDTCs and ATCs identified distinct copy number alterations between the two phenotypes: PDTCs had copy number gains of chromosome 12, whereas ATCs had gains of chromosome 15. Copy number loss was observed on chromosomes 11 and 19 in both tumor types (Fig. 1D). Expression arrays from matched tumors identified numerous dysregulated genes at these specific chromosomal locations as compared with normal thyroid glands from control animals

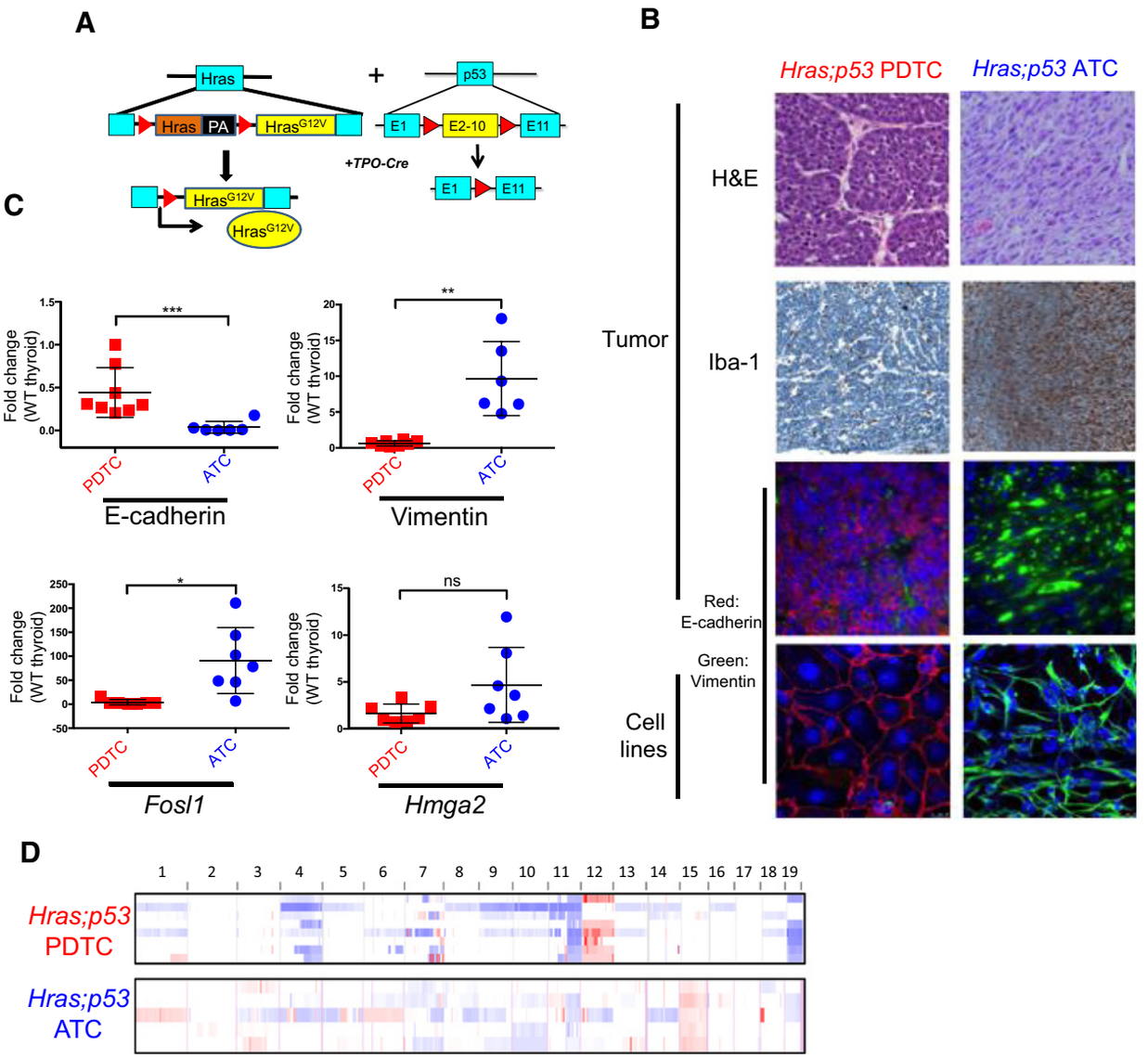

Figure 1.

Tpo-Cre/FR-Hras$^{G12V+/+}$*/p53*$^{f/f}$ mice develop anaplastic and poorly differentiated thyroid cancers. **A,** Scheme of mouse model. Thyroid-specific expression of Cre recombinase driven by *Tpo-Cre* excises the wild-type *Hras* allele, resulting in endogenous expression of *Hras*^{G12V}. Exons 2-10 of *p53* are floxed to inactivate the allele. **B,** Representative sections from *Hras;p53* ATCs and PDTCs. Top three rows, sections of mouse tumors; bottom row, clonal cell lines derived from each tumor type. Shown are hematoxylin and eosin (H&E; ×40), IHC for the macrophage marker Iba-1 (×20), and immunofluorescence for E-cadherin, vimentin, and nuclear staining with DAPI (×20). *Hras;p53* tumor features were retained in the cell lines (×40). **C,** Real-time PCR of the indicated gene products (performed in triplicate) in *Hras;p53* PDTCs and ATCs as compared with wild-type normal thyroid glands (pooled normal samples, $n = 3$; *, $P < 0.05$; **, $P < 0.01$; ***, $P < 0.001$). **D,** aCGH of laser capture microdissected frozen *Hras;p53* PDTCs ($n = 8$) and ATCs ($n = 5$). Red, copy number gain; blue, copy number loss.

(Supplementary File S1). Consistent with their human counterparts, *Hras;p53* murine ATCs were heavily infiltrated with macrophages, resulting in decreased tumor purity and likely accounting for the attenuated copy number signals (Fig. 1B and D). Whole-exome sequencing of 3 ATCs, 3 PDTCs, and one cell line derived from each histotype confirmed loss of sequence reads in the *p53* floxed exons, which was dampened in the ATC tumor, likely because of the extent of the macrophage infiltration, as the ATC cell line showed complete loss of the floxed allele (Supplementary Fig. S1D). There was a trend toward a higher mutation burden in ATCs, although there were no distinguishing patterns of mutations between the two phenotypes (Supplementary Fig. S1E; Supplementary Table S5), as is also the case in human tumors (17).

Growth inhibition of murine PDTCs and ATCs and HRAS-driven thyroid cancer cell lines is attenuated by adaptive resistance to tipifarnib

Treatment of tumor-bearing *Hras;p53* mice with tipifarnib markedly reduced tumor volume as compared with vehicle-

treated controls at 14 days, with modest toxicity manifesting by weight loss (<10% over 2 weeks), although all mice were able to complete the study (Fig. 2A; Supplementary Fig. S2A). A subset of mice showed persistent, although dampened, tumor growth. This occurred despite appropriate inhibition of the target, as determined by Hras defarnesylation, which was suggestive of an adaptive response to tipifarnib (Fig. 2B). We reasoned that adaptation to Hras inhibition may have resulted from release of negative feedback inputs upstream of the oncoprotein, and that this would lead to increased GTP loading of wild-type Ras proteins (22). To confirm the specificity of tipifarnib for targeting HRAS, we mass transfected NIH3T3 cells with myristoylated (irreversibly membrane bound) and nonmyristoylated-$HRAS^{G12V}$, and observed a shift in tipifarnib IC_{50} from 21 nmol/L to 79 nmol/L in myristoylated-$HRAS^{G12V}$–expressing cells (Supplementary Fig. S2B). Next, we treated HRAS-mutant thyroid cancer cell lines C643 and Hth83 with tipifarnib for 12 hours and observed dose-dependent inhibition of ERK phosphorylation (Supplementary Fig. S2C). However, exposure to tipifarnib for 72 hours increased GTP loading of wild-type NRAS and KRAS in the human (Fig. 2C and D) and murine (Supplementary Fig. S2D) *HRAS*-mutant cell lines. Although this was associated with variable effects on ERK phosphorylation (Fig. 2C and D; Supplementary Fig. S2D), we posited that this may blunt the overall efficacy of blocking oncogenic HRAS on downstream signaling. Consistent with this, combined silencing of wild-type NRAS and KRAS inhibited ERK phosphorylation in Hth83 and C643 cells treated with tipifarnib for 72 hours (Fig. 2E and F). We next performed phospho-RTK array assays in Hth83 and C643 after exposure to 100 nmol/L tipifarnib for 72 hours to identify possible upstream inputs responsible for activating wild-type RAS. This showed relatively modest increases in phospho-RTKs (Supplementary Fig. S2E). These results are in stark contrast to the adaptive responses of $BRAF^{V600E}$ thyroid cancer cells to RAF kinase inhibitors, which induce an 11-fold increase in phosphorylation of HER3, due in part to constitutive ligand (neuregulin) expression by these cell lines (19). To define optimal conditions that may drive adaptation of the signaling network to tipifarnib, we explored the transcriptional profile of RTKs and RTK ligands in normal human thyroid tissue, well-differentiated and dedifferentiated human thyroid cancer specimens and thyroid cancer cell lines. We derived a rank-order of ligand-RTK expression in the two *RAS*-mutant cell lines, which was consistent with findings in tumor specimens (Supplementary Fig. S2F). We explored the effects of those top ranked ligands on cell proliferation in the presence and absence of 100 nmol/L tipifarnib in Hth83 and C643 cells (Fig. 2G and H). Although GAS6 and its receptor AXL ranked highly in human and murine thyroid cancers, as well as in thyroid cancer cell lines, exposure to GAS6 did not promote tipifarnib resistance. The Hth83 cell line was most sensitive to EGF, which nearly completely abrogated the growth-inhibitory effects of tipifarnib (Fig. 2G). EGF induced a more potent activation of pEGFR, wild-type RAS-GTP, pAKT, and pMEK in Hth83 cells treated with tipifarnib, which was blocked by the EGFR kinase inhibitor erlotinib, consistent with relief of a negative feedback (Supplementary Fig. S3A). Accordingly, exposure to EGF shifted the tipifarnib dose-response on growth to the right, which was reversed by erlotinib, and by expression of EGFR shRNAs (Supplementary Fig. S3B). In contrast, C643 cells displayed minimal resistance to tipifarnib regardless of ligand exposure, with FGF2 showing some modest effects (Supplementary Fig. S3C). Signaling by FGF2 was augmented in the presence of tipifarnib. Ponatinib, a multikinase inhibitor with activity against FGFR and PDGFR, abrogated the effects of FGF2 on signaling and on cell growth (Supplementary Fig. S3C and S3D).

Exposure of Hth83 and C643 cells to a pooled combination of ligands selected on the basis of their ability to induce growth in the presence of tipifarnib (Fig. 2G and H) resulted in partial resistance to the drug. Combination treatment of tipifarnib with ponatinib abrogated pooled ligand-induced growth in C643 cells, whereas erlotinib was ineffective in Hth83 cells. In contrast, treatment with the allosteric MEK inhibitor AZD6244 enhanced sensitivity to the FTI in both cell lines (Fig. 3A), indicating that blocking signaling downstream of RTK activation may be more effective in overcoming the adaptive resistance to tipifarnib when cells are exposed to multiple ligands, which may be a more accurate reflection of the tumor microenvironment. To extend these observations *in vivo*, we examined RTK and RTK ligand expression in *Hras;p53* murine PDTCs and ATCs (Supplementary Fig. S4A). *Pdgfra, Pdgfrb* and *Fgfr1* were highly expressed in both tumor types, whereas *Egfr* expression was more variable. Treatment of mice with ponatinib or erlotinib did not reduce tumor volumes, and did not improve on the effects of tipifarnib when combined with this drug (Fig. 3B). In contrast, *Hras;p53* mice treated with the tipifarnib/AZD6244 combination had significantly greater reduction of tumor volume at 4 weeks as compared with tipifarnib alone (Fig. 3B and C), which was associated with a dramatic reduction in pERK and Ki67 staining (Fig. 3D). These effects were sustained through 8 weeks in a separate cohort of animals (Supplementary Fig. S4B).

Mechanisms of acquired resistance to tipifarnib

Treatment of tumor-bearing *Hras;p53* mice for up to 6 months with tipifarnib prolonged their survival (Fig. 4A). Despite this, all tumors eventually developed resistance to the drug (Fig. 4B), which was associated with reactivation of Ras downstream signaling (Fig. 4C). To explore potential mechanisms of acquired resistance to tipifarnib, we initially performed whole-exome sequencing of 3 tumors that experienced late growth after an initial response. We found a truncating *Nf1* mutation and an activating *Gnas* mutation (R201S) at high allelic frequencies in two PDTC tumors (Fig. 4D and E; Supplementary Table S6). These mutations were absent in a set of untreated *Hras;p53* ATCs and PDTCs (Supplementary Table S5). Although these mutations were not recurrently seen in other tumors that grew after exposure to tipifarnib ($n = 9$), we explored their functional consequences in greater detail because they pointed to possible on-target effects of the drug on oncogenic *Hras*.

NF1 knockdown partially abrogates the inhibitory effects of tipifarnib on MAPK signaling and induces resistance to the drug

NF1 encodes for a GTPase activating protein and is a negative regulator of RAS (23). The *Nf1* mutation predicts for a protein truncation distal to the central GTPase-activating protein-related domain. Of note, *NF1* loss-of-function mutations in human cancers occur along the entire gene, as illustrated in an institutional pan-cancer clinical cohort (Fig. 4F).

Knockdown of NF1 in C643 and Hth83 cells dampened the inhibitory effects of tipifarnib on MAPK signaling (Fig. 5A).

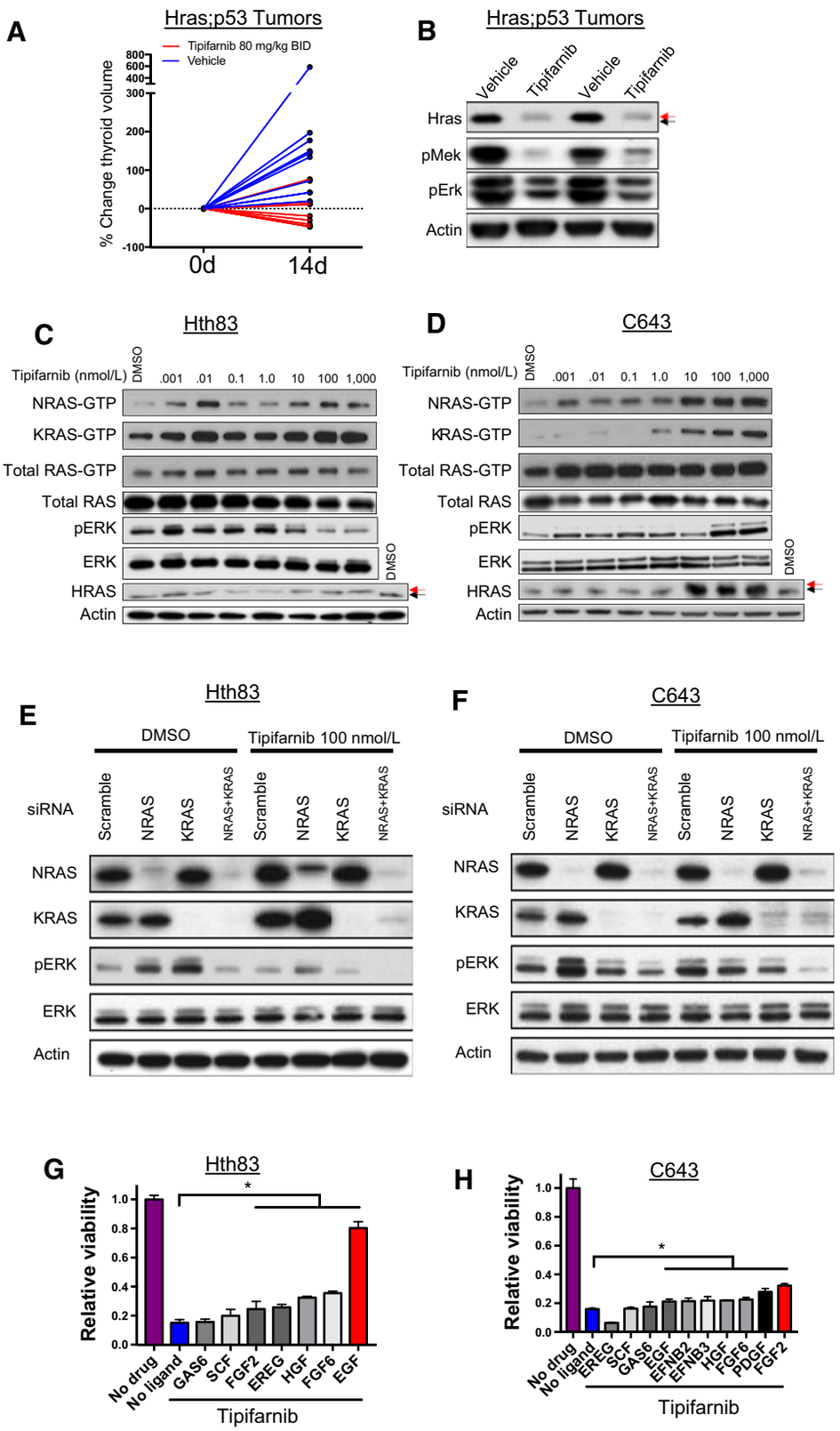

Figure 2.

Adaptive responses to tipifarnib in *Hras*-mutant thyroid cancers. **A,** Tumor-bearing *Hras;p53* mice were treated with vehicle ($n = 9$) or 80 mg/kg twice daily tipifarnib ($n = 6$) for 14 days. Thyroid volume was calculated using 3D ultrasound. **B,** Reduction in pERK and pMEK in *Hras;p53* tumor lysates from mice treated with tipifarnib for 72 hours. Black arrow, farnesylated Hras; red arrow, defarnesylated Hras. **C** and **D,** Western blots of human *HRAS*-mutant thyroid cancer cell lines exposed to increasing concentrations of tipifarnib for 72 hours. Wild-type RAS-GTP levels increase with greater concentrations of tipifarnib. Arrows show molecular weight shift with HRAS defarnesylation. **E** and **F,** Western blot analysis showing a reduction of pERK in tipifarnib-treated C643 and HTH83 cells collected at 72 hours with knockdown of both wild-type RAS proteins. **G,** Effect of exposure to individual ligands for 72 hours on the growth response to 100 nmol/L tipifarnib in Hth83 cells (performed in triplicate). Growth in tipifarnib-treated cells exposed to FGF2, EREG, HGF, FGF6, and EGF was greater than in the absence of ligand (*, $P < 0.05$, t test). **H,** Effects of ligand exposure on response to tipifarnib in C643 cells (performed in triplicate). Growth in the presence of 100 nmol/L tipifarnib was greater after exposure to EGF, EFNB2, EFNB3, HGF, FGF6, PDGF, FGF2 compared with no ligand (*, $P < 0.05$, t test).

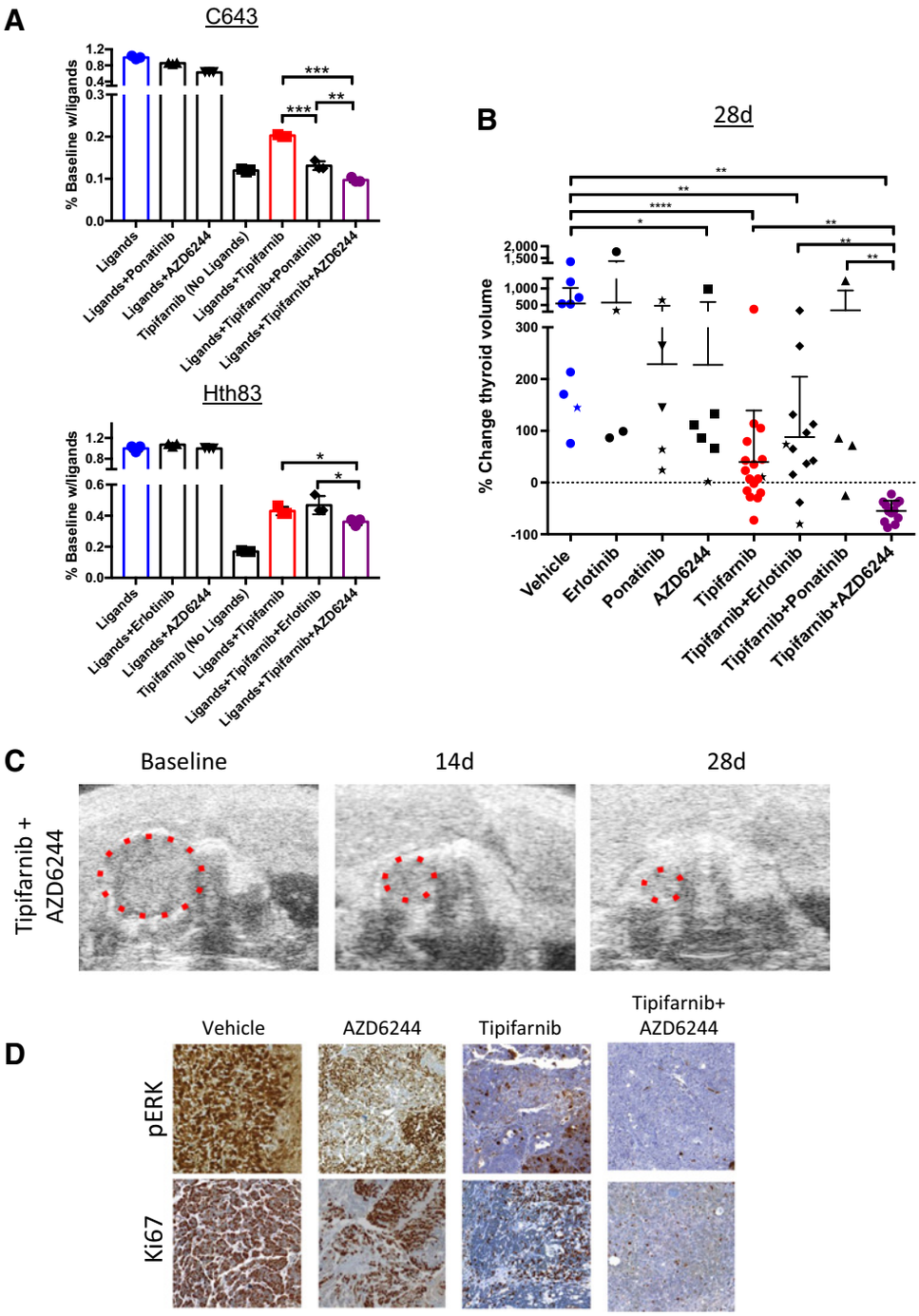

Figure 3.

The MEK inhibitor AZD6244 improves responses to tipifarnib in *Hras*-mutant tumors and cell lines. **A,** Proliferation assays (counted at 6 days, performed in triplicate) in Hras-mutant human cell lines in the presence of a pool of RTK ligands (from Fig. 2G and H with *, $P < 0.05$) and the indicated drugs (tipifarnib 100 nmol/L, erlotinib 25 nmol/L, ponatinib 25 nmol/L, AZD6244 200 nmol/L). Top, C643 cells exposed to FGF2, PDGF, FGF6, HGF, EFNB3, EFNB2, and EGF in 10% serum. **, $P < 0.01$; ***, $P < 0.001$, *t* test. Bottom, Hth83 cells exposed to EGF, FGF6, HGF, EREG, and FGF2 in 10% serum. *$P < 0.05$; *t* test. **B,** Change in thyroid tumor volume as measured by ultrasound in *Hras;p53* mice treated with vehicle ($n = 9$), tipifarnib (80 mg/kg twice daily; $n = 17$), erlotinib (25 mg/kg twice daily; $n = 4$), ponatinib (25 mg/kg once daily; $n = 5$), AZD6244 (25 mg/kg twice daily; $n = 6$) or the indicated combinations (tipifarnib+erlotinib, $n = 12$; tipifarnib+ponatinib, $n = 4$; tipifarnib+AZD6244, $n = 12$) at 28 days. Stars indicate mouse tumor measurements at 14 days in mice that did not survive to 28 days. *, $P < 0.05$; **, $P < 0.01$; ****, $P < 0.0001$, Mann–Whitney test. **C,** Ultrasound images from representative mouse thyroid tumor treated with tipifarnib and AZD6244. **D,** Representative sections of *Hras;p53* tumors stained for pERK and Ki67 treated with the indicated compounds for 28 days (×20). Tissues were collected 2 hours after the last dose.

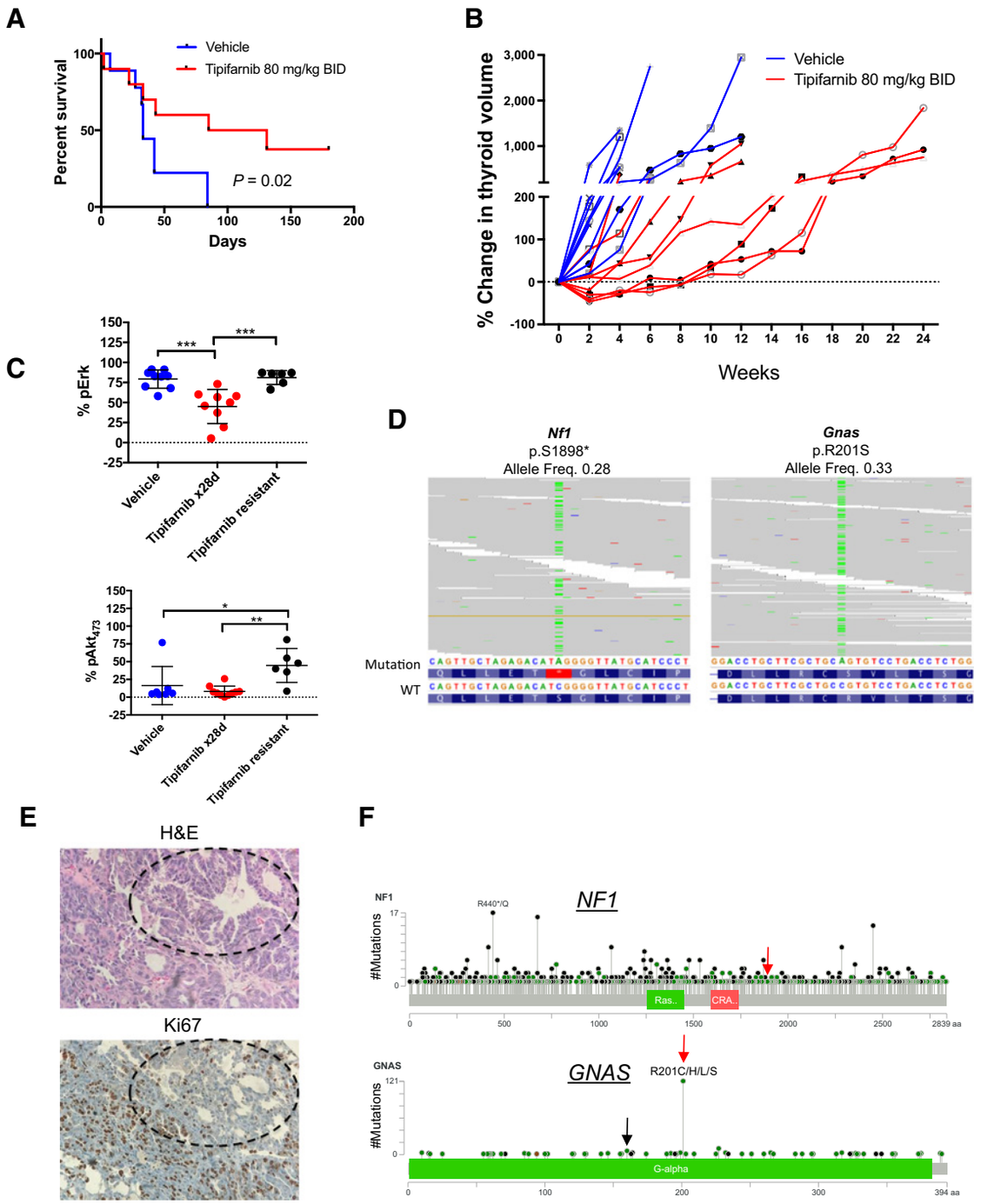

Figure 4.

Nf1 and *Gnas* mutations in tipifarnib-resistant *Hras;p53* tumors. **A,** Tipifarnib ($n = 9$) prolongs survival of tumor-bearing *Hras;p53* mice compared with vehicle ($n = 10$; log-rank $P = 0.02$). **B,** A time course of thyroid volume changes (as measured by ultrasound) in tumor-bearing *Hras;p53* mice treated with vehicle ($n = 10$) or tipifarnib 80 mg/kg twice daily ($n = 9$). **C,** Increased Erk (top) and S473-Akt (bottom) phosphorylation in vehicle ($n = 10$) and tipifarnib-treated tumors (28 days, $n = 9$) and tipifarnib-resistant tumors ($n = 6$; *, $P < 0.05$; **, $P < 0.01$; ***, $P < 0.001$, Mann–Whitney test) as measured by color threshold analysis of IHC-stained tumor sections. **D,** BAM files from whole-exome sequencing of two *Hras;p53* PDTCs, one with a truncating *Nf1* mutation in exon 39 (left) and one with activating R201S mutation in *Gnas* (right). **E,** Hematoxylin and eosin (H&E) and Ki67 of the tipifarnib-resistant mouse tumor with the *Gnas*^{R201S} mutation (×20). Well-differentiated components with lower Ki67 staining (black circles) are identified in proximity to the poorly differentiated elements. **F,** Pan-cancer spectrum of *NF1* and *GNAS* mutations in an institutional clinical cohort undergoing targeted exome sequencing with the MSK-IMPACT panel (54). Red arrows, amino acid changes observed in resistant *Hras;p53* tumors. GNAS^{R201} mutations are the most common. GNAS^{R160} substitutions are also observed in human tumors (black arrow).

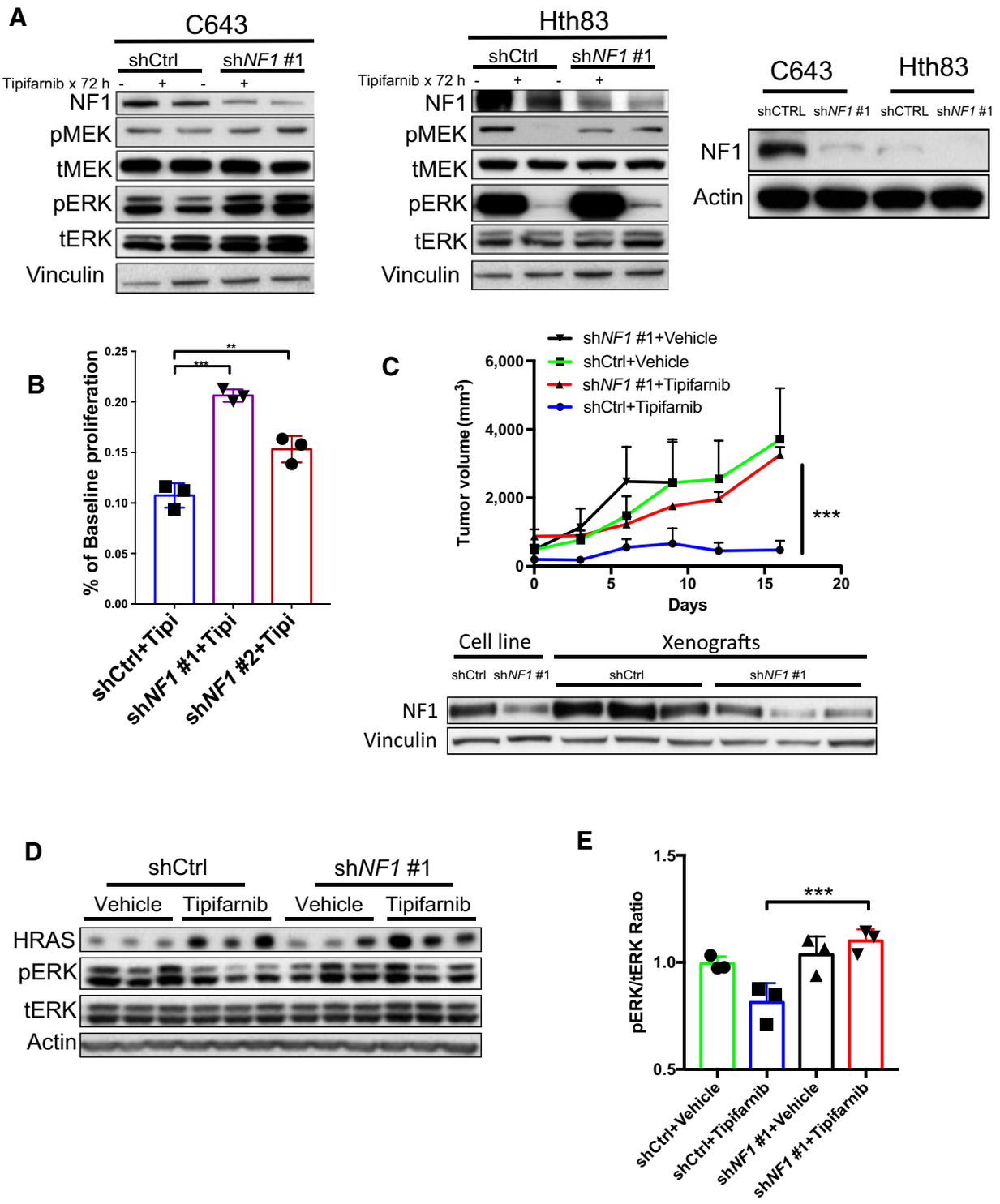

Figure 5.

Knockdown of *NF1* causes resistance to tipifarnib. **A,** Western blot analysis of vehicle or tipifarnib-treated C643 (left) and Hth83 (middle) cells expressing NF1 or control shRNAs. Right, basal expression of NF1 in the two cell lines. **B,** Six-day proliferation assays of C643 cells expressing the indicated short hairpins in the presence of tipifarnib (100 nmol/L), performed in triplicate (*, $P < 0.05$, *t* test). **C,** Top, C643 xenografts with NF1 knockdown are resistant to tipifarnib [shNf1 #1 + tipifarnib vs. shCTRL+ tipifarnib: ***, $P < 0.001$ ($n = 3$ in each group) at 16 days, Mann–Whitney test]. Bottom, Western blot analysis of xenografts demonstrate NF1 knockdown in C643 cells expressing NF1-shRNA. **D,** ERK phosphorylation is increased in tipifarnib-treated C643 xenografts with NF1 knockdown. **E,** Quantification of Western blot analysis in Fig. 5D (***, $P < 0.001$, *t* test).

Hth83 cells are NF1-low, likely explaining the attenuated effects of NF1 knockdown on signaling and growth. Notably, NF1-high C643 cells had a consistently higher IC_{50} than Hth83 cells when tested across several passages (C643 IC_{50}: 11.9 ± 4.7, Hth83 IC_{50}: 5.1 ± 1.98, $n = 5$, $P = 0.02$). NF1 knockdown evoked tipifarnib resistance in C643 cells *in vitro* (Fig. 5B) and *in vivo* (Fig. 5C), and was associated with increased pERK compared with tipifarnib-treated controls (Fig. 5D and E). As the *Nf1* mutation was found in an *Hras;p53* mouse PDTC, we also used CRISPR/Cas9 to induce biallelic loss-of-function *Nf1* mutations in a murine *Hras;p53* PDTC cell line. This eliminated Nf1 protein expression, and resulted in a shift in IC_{50} to tipifarnib from 4 nmol/L to 23 nmol/L (Supplementary Fig. S5A).

Gnas mutations induce tipifarnib resistance *in vivo*, and reactivate a thyroid differentiated transcriptional program

Activating *GNAS* mutations at the R201 position are the most common gain-of-function substitution in human tumors (Fig. 4F), and lie within an exon that is evolutionarily conserved between humans and mice (Supplementary Fig. S6A). The mutant protein encodes for the alpha subunit of the heterotrimeric G protein (Gαs) that activates adenylyl cyclase, which in thyroid cells results in increased expression of thyroid differentiation genes, including those required for thyroid hormone biosynthesis (24) Histology of the *Gnas*-mutant PDTC demonstrated regions with lower Ki67 staining and features consistent with a well-differentiated phenotype, a finding we did not otherwise encounter in untreated *Hras;p53*-mutant cancers (Fig. 4E).

The *GNAS* cluster contains multiple imprinted transcripts, including Gαs and NESP55, preferentially expressed from the maternal allele, and the paternally expressed XLas, A/B and antisense transcripts. We first determined that $G\alpha_{S1}$ was the predominantly expressed transcript in *HRAS*-mutant human and murine cell lines (Supplementary Fig. S6B), and used the mouse homolog as template for generating gain-of-function $Gnas^{R201S}$ (identified in the tipifarnib resistant mouse PDTC) and $Gnas^{R160C}$ constructs, the latter because of its common occurrence in human tumors (Fig. 4F). We studied the *Gnas* mutations in murine cell lines, as the only HRAS-mutant human cell lines are derived from ATCs, and we surmised that some residual potential for redifferentiation might be necessary to observe an effect from the *Gnas* mutations.

PDTC (E-cadherin positive) allografts derived from *Hras;p53*–mutant cell lines transduced with either of the *Gnas* mutants were resistant to tipifarnib (Fig. 6A). Vector-transduced *Hras;p53* allografts showed inhibition of pERK in response to tipifarnib. In contrast, and consistent with the known inhibitory effects of cAMP activation on MAPK signaling, baseline pERK was lower in the $Gnas^{R201S}$-transduced allografts, and not further inhibited by tipifarnib. However, there was an increase in pCreb, a protein kinase A substrate, in $Gnas^{R201S}$-transduced, but not in vector-transduced allografts treated with tipifarnib, consistent with activation of cAMP-dependent signaling, a pathway that promotes growth and differentiation of normal thyrocytes (Fig. 6B).

In contrast, expression of the *Gnas* mutants did not significantly dampen the growth-inhibitory effects of tipifarnib in *Hras;p53* (E-cadherin–negative) ATCs (Supplementary Fig. S7A) and failed to induce CREB phosphorylation (Supplementary Fig. S7B). RNA sequencing of *Hras;p53* PDTC and ATC allografts showed that tipifarnib reduced expression of ERK signature genes in both tumor types (Fig. 6C). However, a transcriptional signature of thyroid differentiation was induced by tipifarnib only in PDTCs, an effect that was further augmented in *Hras;p53* PDTCs expressing $Gnas^{R201S}$ (Fig. 6C–E). Importantly, expression of *Nkx2-1* and *Pax8*, master regulators of thyroid differentiation, was increased in cells transduced with $Gnas^{R201S}$ (Fig. 6E).

Discussion

The requirement of RAS association with cellular membranes for signaling is well established (25). This is promoted through posttranslational modifications of the RAS C-terminal CAAX motif. The initial and obligate step in this process is catalyzed through farnesyltransferase, which attaches a farnesyl isoprenoid lipid to the cysteine of the CAAX box. This prompted efforts to develop effective FTIs, which were later found to be ineffective against KRAS and NRAS, as these become substrates for geranyl-geranyltransferase 1, allowing them to associate with membranes and remain functional (9). However, HRAS is effectively delocalized by FTIs, disrupting its signaling and biological action (10). The relative rarity of *HRAS* mutations in cancers raised questions on whether it is a *bona fide* oncogenic driver and a legitimate therapeutic target (26), despite experimental evidence pointing to distinct transforming potency of mutant RAS isoforms in different cell lineages (27). Several lines of evidence should now dispel these concerns: (i) Mutations of *HRAS* are mutually exclusive with other driver mutations signaling along the MAPK pathway in thyroid and other malignancies (28); (ii) Endogenous expression of $Hras^{G12V}$ drives murine thyroid tumorigenesis in the context of *Nf2*, *Pten*, or *p53* loss (29); (iii) as shown here, acquired resistance to Hras delocalization can be mediated by loss-of-function mutations of *Nf1*, which when absent derepresses Ras signaling to induce transformation (30).

FTIs can also disrupt other farnesylated proteins, which could contribute to the efficacy and/or toxicity of the drugs. Among these, the two mammalian Rheb isoforms, Rheb1 and Rheb2, have received particular attention, as they are critical components of the PI3K–Akt–TSC–mTOR pathway. In its GTP-bound state, Rheb activates the rapamycin-sensitive mTOR complex (mTORC1), a step that is inhibited by FTIs (31). Other relevant farnesylated proteins include the centromere-binding proteins CEBP-E and CEBP-F. Upon treatment with FTIs, CEBP-E no longer associates with microtubules, which results in accumulation of cells in metaphase (32, 33). However, our current report points to Hras as the key therapeutic target of tipifarnib in the context of tumors harboring *Hras* mutations. Consistent with results using genetic targeting of oncogenic RAS, treatment with tipifarnib resulted in GTP loading of wild-type RAS, which reactivated downstream signaling (22). Even more telling was the fact that acquired resistance to tipifarnib was associated with a *de novo* inactivating mutation of *Nf1*. Although these data point to oncogenic Hras as the primary target of tipifarnib in this setting, we cannot exclude that other farnesylated proteins may have contributed to its effects.

Although tipifarnib induced clear responses and extended survival of mice with Hras-driven thyroid cancers, in most cases, the drug stabilized the disease or dampened tumor growth. As mentioned, Hras delocalization was associated with activation of wild-type RAS and adaptive resistance to the

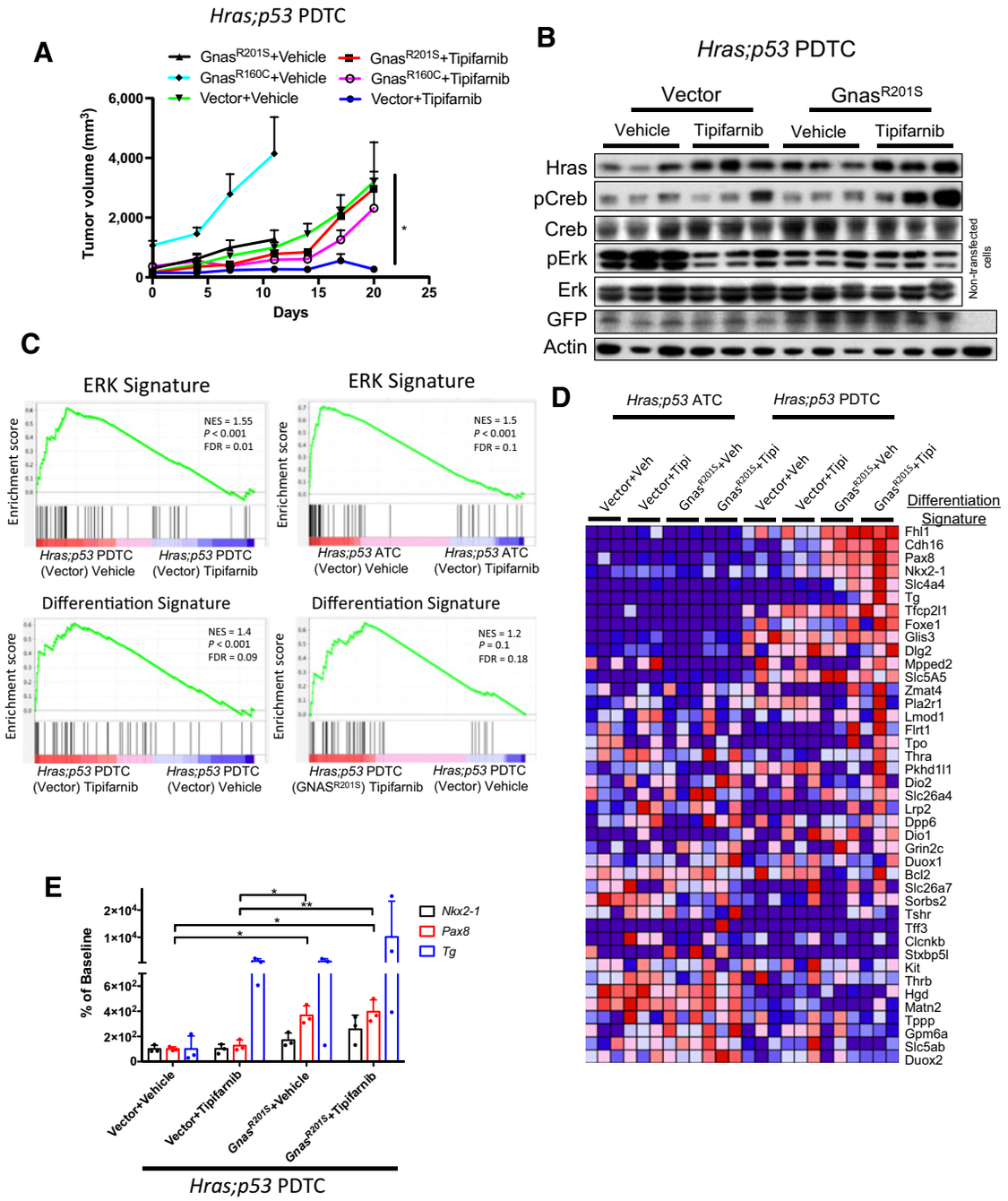

Figure 6.

Mutations in Gnas drive resistance to tipifarnib and activate a transcriptional program of thyroid differentiation. **A,** *Hras;p53* PDTC allografts (in nude mice) transduced with *Gnas* mutants R160C and R201S are resistant to tipifarnib (80 mg/kg twice daily; tipifarnib-treated: $Gnas^{R201S}$ vs. vector, *, $P < 0.05$; $Gnas^{R160C}$ vs. vector, *, $P < 0.05$, Mann–Whitney test; $n = 5$ all conditions). **B,** Western blot analysis of vehicle or tipifarnib-treated *Hras;p53*/vector or *Hras;p53*/$Gnas^{R201S}$ allograft lysates (from **A**) show increased pCreb in tipifarnib-treated tumors expressing $Gnas^{R201S}$. The vector contains an IRES-GFP sequence. **C,** Top, GSEA plots showing significant reduction of a 52 gene ERK signature in vector–transduced *Hras;p53* ATC and PDTC allografts treated with tipifarnib. Bottom, tipifarnib treatment of *Hras;p53* PDTC allografts results in enrichment of thyroid differentiation genes, which is augmented in *Hras;p53* tumors transduced with $Gnas^{R201S}$ as compared with vehicle-treated vector controls. The Differentiation Signature is based on the Thyroid Differentiation Score identified in the TCGA study of papillary thyroid cancer (28). **D,** RNA-seq of vehicle or tipifarnib-treated vector or $Gnas^{R201S}$-transduced *Hras;p53* PDTC and ATC allografts shows enrichment of thyroid differentiation genes in response to tipifarnib in Gnas-transduced PDTC allografts. **E,** Pax8, Nkx2.1, and Tg expression levels measured by real-time PCR. Tg is enhanced in 2/3 *Hras;p53* PDTC allografts treated with tipifarnib, confirming the RNA-seq data and consistent with samples with higher Creb phosphorylation (**B**). Pax8 expression was greater in cells transduced with $Gnas^{R201S}$ (*, $P < 0.05$; **, $P < 0.01$, *t* test).

drug, which could be overcome *in vitro* by blocking distinct upstream RTKs driving wild-type RAS activation. As opposed to BRAF-mutant thyroid cancer cells, where activation of the NRG1-HER3/HER2 pathway is primarily responsible for relief of negative feedback in response to RAF or MEK inhibition (19), the RTK responses were relatively modest and heterogeneous in the HRAS context. Accordingly, neither erlotinib nor ponatinib, which showed some activity *in vitro*, were effective alone or in combination with tipifarnib *in vivo*. It may be that a combination of upstream inputs drives adaptive responses to the drug in this setting. In contrast, combination of tipifarnib with the MEK inhibitor AZD6244 (selumetinib) was remarkably effective. This is consistent with maintenance of tumor viability via Hras-independent reactivation of MAPK signaling after treatment with the FTI. Newer allosteric MEK inhibitors, such as trametinib, inhibit ERK more potently than selumetinib in *RAS-mutant* contexts, and may ultimately prove to be preferable in combination with tipifarnib for HRAS-mutant disease (34). Whereas *HRAS*-mutant thyroid cancers are observed less frequently than *BRAF* or *NRAS*, they are present in sufficient numbers that have enabled basket clinical trials with tipifarnib, which are ongoing.

Upon treatment with FTIs, Hras accumulates as a cytoplasmic defarnesylated pool. We found that the accumulation of the defarnesylated HRAS varied considerably in tipifarnib-treated Hras-mutant human and mouse models, with some cells exhibiting decreased levels and others higher levels of the protein (25). We currently have no explanation for this variability. Besides farnesylation, HRAS plasma membrane localization requires palmitoylation on two cysteines immediately upstream of the CAAX motif (35). Depalmitoylation at the plasma membrane in turn initiates recycling of HRAS to endomembranes. This pool of defarnesylated mutant HRAS could relocate to the plasma membrane and attenuate effects of FTIs depending on the pharmacokinetics of the drug and its bioavailability, and may also explain the dampened response to the drug *in vivo*. The cycle of depalmitoylation and repalmitoylation, which regulates HRAS and NRAS subcellular trafficking, can be interrupted by the acyl protein thioesterase 1 (APT1) inhibitor palmostatin B (36). Treatment with this drug randomizes Ras localization to all membranes, and was shown to induce partial phenotypic reversion in oncogenic $HRas^{G12V}$-transformed fibroblasts (36) and in $Nras^{G12D}$-transduced hematopoietic cells (37). Conceivably, combination therapy with a farnesyl transferase and an APT1 inhibitor may achieve more profound and sustained Hras delocalization, and if tolerated, improve responses.

Prolonged treatment of Hras-mutant tumors with tipifarnib resulted in emergence of a resistant tumor that harbored a nonsense mutation in *Nf1*. As would be predicted on the basis of their common mechanism of action, *RAS* and *NF1* are mutually exclusive in most cancers, including those of the thyroid (17, 28). Loss of function of *NF1* also confers resistance to other therapies that indirectly target the RAS signaling pathway, including RAF inhibitors in melanoma, and EGFR kinase inhibitors in lung cancer (38–40).

In addition to *Nf1* loss, we identified a canonical activating mutation of *Gnas* in a resistant tumor, which when transduced into $Hras^{G12V}$ mouse thyroid tumor cells generated resistance to tipifarnib. *GNAS* mutations were first identified in growth hormone–secreting pituitary tumors (41), and subsequently in autonomously functioning thyroid nodules (42), mucin-producing IPMNs, and appendiceal cancers (43, 44). The $GNAS^{R201S}$ mutation reduces GTP hydrolysis of $G\alpha_s$, and leads to constitutive activation of adenylyl cyclase and generation of cAMP (41). In thyroid cells, the cAMP signaling pathway induces cell growth and expression of genes required for thyroid hormone biosynthesis. Accordingly, $Gnas^{R201S}$-transduced *Hras;p53* PDTC cells exhibited increased expression of a thyroid differentiation transcriptional program. Treatment with tipifarnib further potentiated cAMP signaling, as measured by phosphorylated Creb, and was associated with greater expression of thyroid-specific iodine metabolism genes.

In well-differentiated thyroid cancers the transcriptional output of the MAPK pathway is inversely correlated with the expression of genes involved in iodide transport and thyroid hormone biosynthesis, which as mentioned are regulated by cAMP-dependent signaling (28). This reciprocal relationship has been exploited in the clinic, as treatment of *BRAF*- or *RAS*-mutant thyroid cancers with RAF or MEK inhibitors restores iodide transport, and responsiveness to radioiodine therapy (45–48). The cAMP–protein kinase A pathway suppresses MAPK signaling in many cell types, primarily through inhibition of CRAF (49). Conversely, there is global silencing of thyroid-differentiated function when MAPK is constitutively activated (Fig. 7A–C; refs. 45, 50). Enforced overexpression of RAS or of a constitutively active RAF protein in thyroid FRTL5 cells decreases the transcriptional activity of Nkx2-1 (TTF-1), a homeodomain-containing transcription factor required for normal thyroid development and expression of thyroid-specific proteins (51, 52). Hence, acquisition of a *Gnas* mutation in response to tipifarnib inhibition of MAPK signaling restores cAMP control of cell growth, and returns thyroid cells to a more differentiated state. Interestingly, activation of a cAMP-dependent melanocytic signaling network can generate resistance to RAF inhibitors in melanoma cells, suggesting that this may be a common property of cell lineages dependent on cAMP for differentiated function (53). All of these prior situations result from adaptive responses of the signaling network to MAPK pathway inhibitors. The discovery of a gain-of-function *Gnas* mutation, which constitutively activates cAMP signaling, in a tipifarnib-resistant tumor is the first demonstration that this mechanism of escape from MAPK blockade can also arise as a result of a somatic mutation.

The resistance mutations we found were of interest because of their functional consequences, however it is legitimate to ask why they were not recurrent, as few acquired resistance mutations were identified in the tumors we studied (we also found a clonal mutation of *Arid1b* in one additional sample). We believe that the most likely explanation is that these cancers exhibit significant adaptive resistance to the drug, which is best illustrated by the markedly improved and more durable responses to combined tipifarnib-AZD6244 treatment. Thus, tipifarnib alone may not exert sufficient selective pressure for higher frequency acquisition of *de novo* resistance mutations.

Collectively, these findings demonstrate that FTIs specifically target the HRAS oncoprotein and that reactivation of RAS signaling through adaptive responses or through acquired genomic changes can limit their effectiveness. As clinical trials with tipifarnib are currently accruing for patients with

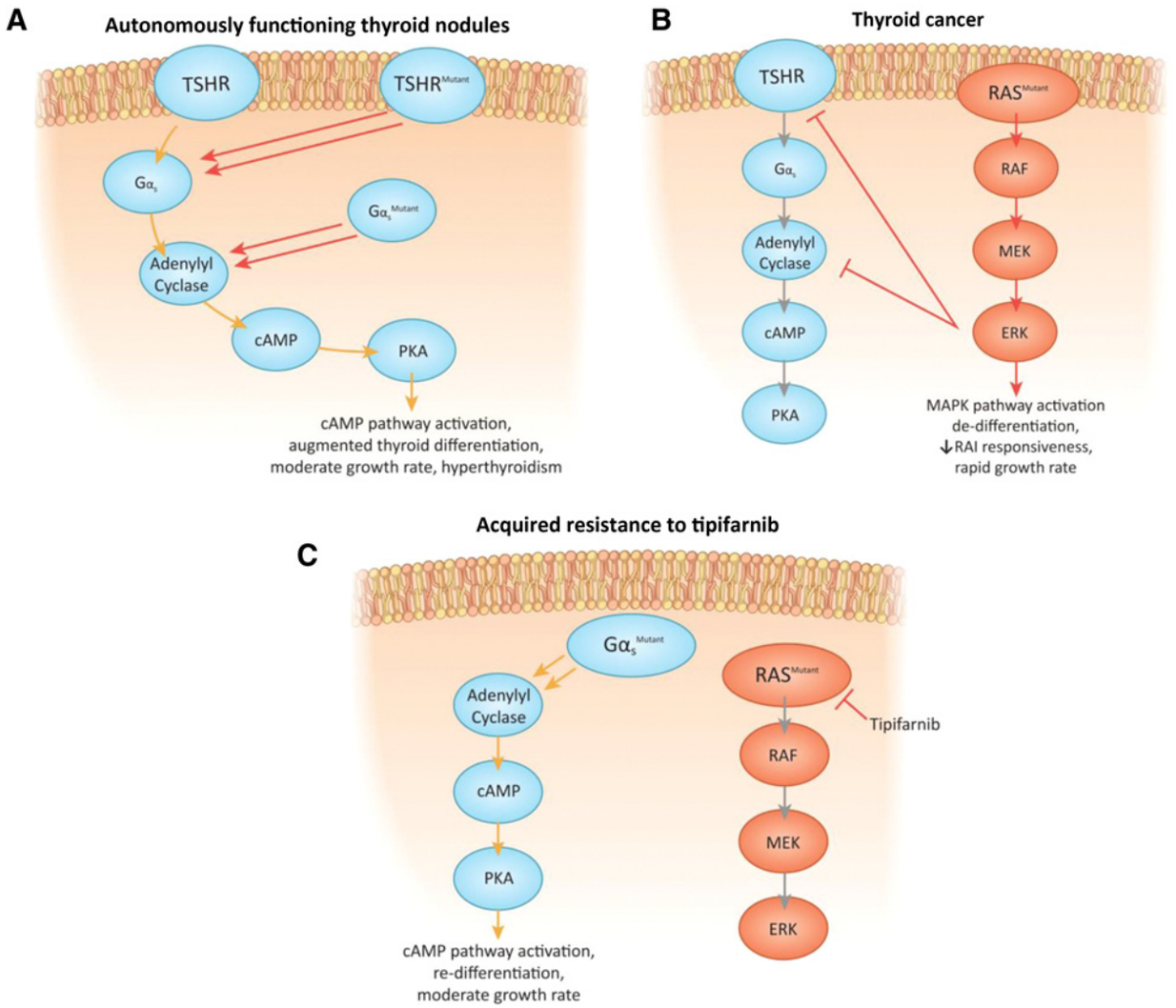

Figure 7.

Acquired resistance to tipifarnib by Gnas activating mutations. Reciprocal relationship between MAPK activation and cAMP signaling in thyroid cancer. **A,** Activating mutations of the TSH receptor or GNAS induce growth and differentiated function in autonomously functioning thyroid adenomas. **B,** Constitutive activation of MAPK by oncogenic RAS inhibits TSH-dependent cAMP signaling at multiple levels (RAI, radioactive iodine; ref. 50). **C,** Acquisition of a *Gnas* mutation with long-term tipifarnib exposure reactivates cAMP signaling, partially restoring differentiated gene expression and cell growth.

HRAS-mutant malignancies, and efforts are underway to develop compounds targeting other RAS isoforms, these results will help inform the design of subsequent rational combination strategies.

Disclosure of Potential Conflicts of Interest

B.R. Untch has ownership interest [including patents in an MSK patent (MSK Ref. SK 2014-024-03; title: treatment of H-Ras-driven tumors)]. J.A. Knauf has ownership interest (including patents) in an MSK patent (MSK Ref. SK 2014-024-03; title: treatment of H-Ras-driven tumors). A.L. Ho is a consultant/advisory board member for Merck, BMS, Eisai, Genzyme, Novartis, Regeneron, Sun Pharmaceuticals, Sanofi Aventis. J.A. Fagin has ownership interest (including patents) in an MSK patent (MSK Ref. SK 2014-024-03; title: treatment of H-Ras-driven tumors; application number: 15/305,788). No potential conflicts of interest were disclosed by the other authors.

Authors' Contributions

Conception and design: B.R. Untch, J.A. Knauf, J.A. Fagin
Development of methodology: B.R. Untch, M.E.R. Garcia-Rendueles, G.P. Krishnamoorthy, M. Saqcena, J.A. Fagin
Acquisition of data (provided animals, acquired and managed patients, provided facilities, etc.): B.R. Untch, V.D. Anjos, M.E.R. Garcia-Rendueles, J.A. Knauf, U.K. Bhanot
Analysis and interpretation of data (e.g., statistical analysis, biostatistics, computational analysis): B.R. Untch, V.D. Anjos, M.E.R. Garcia-Rendueles, G.P. Krishnamoorthy, M. Saqcena, N.D. Socci, R. Ghossein, J.A. Fagin
Writing, review, and/or revision of the manuscript: B.R. Untch, V.D. Anjos, M.E.R. Garcia-Rendueles, A.L. Ho, R. Ghossein, J.A. Fagin
Administrative, technical, or material support (i.e., reporting or organizing data, constructing databases): B.R. Untch, V.D. Anjos
Study supervision: B.R. Untch, J.A. Fagin
Other (provided expertise on micro-dissection of tissue samples): U.K. Bhanot

Acknowledgments

This work was supported by NIH P50-CA72012 (to J.A. Fagin), P30-CA008748 (Memorial Sloan Kettering), RO1-CA72597 (to J.A. Fagin), RO1-CA50706 (to J.A. Fagin) and grants from the American Thyroid Association (to B.R. Untch), the American Surgical Association Foundation (to B.R. Untch), the Paul LoGerfo Research Award from the American Association of Endocrine Surgeons (to B.R. Untch) and the Charles A Dana Foundation/ T32 5T32CA009512 (to B.R. Untch). We thank the MSKCC Research Animal Resource Center and the following core labs for their support: Small Animal Imaging, Molecular Cytology, Bioinformatics, Pathology, the Integrative Genomics Operation funded by Cycle for Survival and the Marie-Josée and Henry R. Kravis Center for Molecular Oncology. These studies were performed under a collaboration agreement with Kura Oncology, Inc.

The costs of publication of this article were defrayed in part by the payment of page charges. This article must therefore be hereby marked *advertisement* in accordance with 18 U.S.C. Section 1734 solely to indicate this fact.

Received June 27, 2017; revised January 11, 2018; accepted May 9, 2018; published first May 14, 2018.

References

1. Shima F, Matsumoto S, Yoshikawa Y, Kawamura T, Isa M, Kataoka T. Current status of the development of Ras inhibitors. J Biochem 2015; 158:91–9.
2. Ostrem JM, Shokat KM. Direct small-molecule inhibitors of KRAS: from structural insights to mechanism-based design. Nat Rev Drug Discov 2016; 15:771–85.
3. Fukahori M, Yoshida A, Hayashi H, Yoshihara M, Matsukuma S, Sakuma Y, et al. The associations between RAS mutations and clinical characteristics in follicular thyroid tumors: new insights from a single center and a large patient cohort. Thyroid 2012;22:683–9.
4. Volante M, Rapa I, Gandhi M, Bussolati G, Giachino D, Papotti M, et al. RAS mutations are the predominant molecular alteration in poorly differentiated thyroid carcinomas and bear prognostic impact. J Clin Endocrinol Metab 2009;94:4735–41.
5. Ricarte-Filho JC, Ryder M, Chitale DA, Rivera M, Heguy A, Ladanyi M, et al. Mutational profile of advanced primary and metastatic radioactive iodine-refractory thyroid cancers reveals distinct pathogenetic roles for BRAF, PIK3CA, and AKT1. Cancer Res 2009;69:4885–93.
6. Moura MM, Cavaco BM, Pinto AE, Leite V. High prevalence of RAS mutations in RET-negative sporadic medullary thyroid carcinomas. J Clin Endocrinol Metab 2011;96:E863–8.
7. Agrawal N, Frederick MJ, Pickering CR, Bettegowda C, Chang K, Li RJ, et al. Exome sequencing of head and neck squamous cell carcinoma reveals inactivating mutations in NOTCH1. Science 2011;333:1154–7.
8. Cancer Genome Atlas Research Network. Comprehensive molecular characterization of urothelial bladder carcinoma. Nature 2014;507:315–22.
9. Whyte DB, Kirschmeier P, Hockenberry TN, Nunez-Oliva I, James L, Catino JJ, et al. K- and N-Ras are geranylgeranylated in cells treated with farnesyl protein transferase inhibitors. J Biol Chem 1997;272:14459–64.
10. Chen X, Makarewicz JM, Knauf JA, Johnson LK, Fagin JA. Transformation by Hras(G12V) is consistently associated with mutant allele copy gains and is reversed by farnesyl transferase inhibition. Oncogene 2014;33:5442–9
11. End DW, Smets G, Todd AV, Applegate TL, Fuery CJ, Angibaud P, et al. Characterization of the antitumor effects of the selective farnesyl protein transferase inhibitor R115777 in vivo and in vitro. Cancer Res 2001;61: 131–7.
12. Berndt N, Hamilton AD, Sebti SM. Targeting protein prenylation for cancer therapy. Nat Rev Cancer 2011;11:775–91.
13. Brunner TB, Hahn SM, Gupta AK, Muschel RJ, McKenna WG, Bernhard EJ. Farnesyltransferase inhibitors: an overview of the results of preclinical and clinical investigations. Cancer Res 2003;63:5656–68.
14. Kusakabe T, Kawaguchi A, Kawaguchi R, Feigenbaum L, Kimura S. Thyrocyte-specific expression of Cre recombinase in transgenic mice. Genesis 2004;39:212–6.
15. Jonkers J, Meuwissen R, van der Gulden H, Peterse H, van der Valk M, Berns A. Synergistic tumor suppressor activity of BRCA2 and p53 in a conditional mouse model for breast cancer. Nat Genet 2001;29:418–25.
16. Chen X, Mitsutake N, LaPerle K, Akeno N, Zanzonico P, Longo VA, et al. Endogenous expression of Hras(G12V) induces developmental defects and neoplasms with copy number imbalances of the oncogene. Proc Natl Acad Sci U S A 2009;106:7979–84.
17. Landa I, Ibrahimpasic T, Boucai L, Sinha R, Knauf JA, Shah RH, et al. Genomic and transcriptomic hallmarks of poorly differentiated and anaplastic thyroid cancers. J Clin Invest 2016;126:1052–66.
18. Lemmon MA, Schlessinger J. Cell signaling by receptor tyrosine kinases. Cell 2010;141:1117–34.
19. Montero-Conde C, Ruiz-Llorente S, Dominguez JM, Knauf JA, Viale A, Sherman EJ, et al. Relief of feedback inhibition of HER3 transcription by RAF and MEK inhibitors attenuates their antitumor effects in BRAF-mutant thyroid carcinomas. Cancer Discov 2013;3:520–33.
20. Shalem O, Sanjana NE, Hartenian E, Shi X, Scott DA, Mikkelson T, et al. Genome-scale CRISPR-Cas9 knockout screening in human cells. Science 2014;343:84–7.
21. Pratilas CA, Taylor BS, Ye Q, Viale A, Sander C, Solit DB, et al. (V600E)BRAF is associated with disabled feedback inhibition of RAF-MEK signaling and elevated transcriptional output of the pathway. Proc Natl Acad Sci U S A 2009;106:4519–24.
22. Young A, Lou D, McCormick F. Oncogenic and wild-type Ras play divergent roles in the regulation of mitogen-activated protein kinase signaling. Cancer Discov 2013;3:112–23.
23. Ratner N, Miller SJ. A RASopathy gene commonly mutated in cancer: the neurofibromatosis type 1 tumour suppressor. Nat Rev Cancer 2015;15: 290–301.
24. Parma J, Duprez L, Van Sande J, Hermans J, Rocmans P, Van Vliet G, et al. Diversity and prevalence of somatic mutations in the thyrotropin receptor and Gs alpha genes as a cause of toxic thyroid adenomas. J Clin Endocrinol Metab 1997;82:2695–701.
25. Cox AD, Der CJ, Philips MR. Targeting RAS membrane association: back to the future for anti-RAS drug discovery? Clin Cancer Res 2015;21:1819–27.
26. Cox AD, Fesik SW, Kimmelman AC, Luo J, Der CJ. Drugging the undruggable RAS: Mission possible? Nat Rev Drug Discov 2014;13:828–51.
27. Castellano E, Santos E. Functional specificity of ras isoforms: so similar but so different. Genes Cancer 2011;2:216–31.
28. Cancer Genome Atlas Research Network. Integrated genomic characterization of papillary thyroid carcinoma. Cell 2014;159:676–90.
29. Garcia-Rendueles ME, Ricarte-Filho JC, Untch BR, Landa I, Knauf JA Voza F, et al. NF2 loss promotes oncogenic RAS-induced thyroid cancers via YAP-dependent transactivation of RAS proteins and sensitizes them to MEK inhibition. Cancer Discov 2015;5:1178–93.
30. Bollag G, Clapp DW, Shih S, Adler F, Zhang YY, Thompson P, et al. Loss of NF1 results in activation of the Ras signaling pathway and leads to aberrant growth in haematopoietic cells. Nat Genet 1996;12:144–8.
31. Castro AF, Rebhun JF, Clark GJ, Quilliam LA. Rheb binds tuberous sclerosis complex 2 (TSC2) and promotes S6 kinase activation in a rapamycin- and farnesylation-dependent manner. J Biol Chem 2003;278:32493–6.
32. Ashar HR, James L, Gray K, Carr D, Black S, Armstrong L, et al. Farnesyl transferase inhibitors block the farnesylation of CENP-E and CENP-F and alter the association of CENP-E with the microtubules. J Biol Chem 2000;275:30451–7.
33. Crespo NC, Ohkanda J, Yen TJ, Hamilton AD, Sebti SM. The farnesyltransferase inhibitor, FTI-2153, blocks bipolar spindle formation and chromosome alignment and causes prometaphase accumulation during mitosis of human lung cancer cells. J Biol Chem 2001;276:16161–7.
34. Lito P, Saborowski A, Yue J, Solomon M, Joseph E, Gadal S, et al. Disruption of CRAF-mediated MEK activation is required for effective MEK inhibition in KRAS mutant tumors. Cancer Cell 2014;25:697–710.
35. Hancock JF, Paterson H, Marshall CJ. A polybasic domain or palmitoylation is required in addition to the CAAX motif to localize p21ras to the plasma membrane. Cell 1990;63:133–9.
36. Dekker FJ, Rocks O, Vartak N, Menninger S, Hedberg C, Balamurugan R, et al. Small-molecule inhibition of APT1 affects Ras localization and signaling. Nat Chem Biol 2010;6:449–56.

37. Xu J, Hedberg C, Dekker FJ, Li Q, Haigis KM, Hwang E, et al. Inhibiting the palmitoylation/depalmitoylation cycle selectively reduces the growth of hematopoietic cells expressing oncogenic Nras. Blood 2012; 119:1032–5.
38. de Bruin EC, Cowell C, Warne PH, Jiang M, Saunders RE, Melnick MA, et al. Reduced NF1 expression confers resistance to EGFR inhibition in lung cancer. Cancer Discov 2014;4:606–19.
39. Whittaker SR, Theurillat JP, Van Allen E, Wagle N, Hsiao J, Cowley GS, et al. A genome-scale RNA interference screen implicates NF1 loss in resistance to RAF inhibition. Cancer Discov 2013;3:350–62.
40. Beauchamp EM, Woods BA, Dulak AM, Tan L, Xu C, Gray NS, et al. Acquired resistance to dasatinib in lung cancer cell lines conferred by DDR2 gatekeeper mutation and NF1 loss. Mol Cancer Ther 2014;13: 475–82.
41. Landis CA, Masters SB, Spada A, Pace AM, Bourne HR, Vallar L. GTPase inhibiting mutations activate the alpha chain of Gs and stimulate adenylyl cyclase in human pituitary tumours. Nature 1989;340:692–6.
42. Lyons J, Landis CA, Harsh G, Vallar L, Grunewald K, Feichtinger H, et al. Two G protein oncogenes in human endocrine tumors. Science 1990; 249:655–9.
43. Wu J, Matthaei H, Maitra A, Dal Molin M, Wood LD, Eshleman JR, et al. Recurrent GNAS mutations define an unexpected pathway for pancreatic cyst development. Sci Transl Med 2011;3:92ra66.
44. Nishikawa G, Sekine S, Ogawa R, Matsubara A, Mori T, Taniguchi H, et al. Frequent GNAS mutations in low-grade appendiceal mucinous neoplasms. Br J Cancer 2013;108:951–8.
45. Chakravarty D, Santos E, Ryder M, Knauf JA, Liao XH, West BL, et al. Small-molecule MAPK inhibitors restore radioiodine incorporation in mouse thyroid cancers with conditional BRAF activation. J Clin Invest 2011;121: 4700–11.
46. Nagarajah J, Le M, Knauf JA, Ferrandino G, Montero-Conde C, Pillarsetty N, et al. Sustained ERK inhibition maximizes responses of BrafV600E thyroid cancers to radioiodine. J Clin Invest 2016;126: 4119–24.
47. Ho AL, Grewal RK, Leboeuf R, Sherman EJ, Pfister DG, Deandreis D, et al. Selumetinib-enhanced radioiodine uptake in advanced thyroid cancer. N Engl J Med 2013;368:623–32.
48. Rothenberg SM, McFadden DG, Palmer EL, Daniels GH, Wirth LJ. Redifferentiation of iodine-refractory BRAF V600E-mutant metastatic papillary thyroid cancer with dabrafenib. Clin Cancer Res 2015;21:1028–35.
49. Dumaz N, Marais R. Integrating signals between cAMP and the RAS/RAF/MEK/ERK signalling pathways. Based on the anniversary prize of the Gesellschaft fur Biochemie und Molekularbiologie Lecture delivered on 5 July 2003 at the Special FEBS Meeting in Brussels. FEBS J 2005;272:3491–504.
50. Wang J, Knauf JA, Basu S, Puxeddu E, Kuroda H, Santoro M, et al. Conditional expression of RET/PTC induces a weak oncogenic drive in thyroid PCCL3 cells and inhibits thyrotropin action at multiple levels. Mol Endocrinol 2003;17:1425–36.
51. Missero C, Pirro MT, Di Lauro R. Multiple ras downstream pathways mediate functional repression of the homeobox gene product TTF-1. Mol Cell Biol 2000;20:2783–93.
52. Velasco JA, Acebro NA, Zannini M, Mart INPRJ, Di Lauro R, Santisteban P. Ha-ras interference with thyroid cell differentiation is associated with a down-regulation of thyroid transcription factor-1 phosphorylation. Endocrinology 1998;139:2796–802.
53. Johannessen CM, Johnson LA, Piccioni F, Townes A, Frederick DT, Donahue MK, et al. A melanocyte lineage program confers resistance to MAP kinase pathway inhibition. Nature 2013;504:138–42.
54. Cheng DT, Mitchell TN, Zehir A, Shah RH, Benayed R, Syed A, et al. Memorial sloan kettering-integrated mutation profiling of actionable cancer targets (MSK-IMPACT): a hybridization capture-based next-generation sequencing clinical assay for solid tumor molecular oncology. J Mol Diagn 2015;17:251–64.